

The unification of powerful quasars and radio galaxies and their relation to other massive galaxies

Pece Podigachoski and Peter Barthel

Kapteyn Astronomical Institute, University of Groningen, 9747 AD Groningen, The Netherlands

podigachoski@astro.rug.nl

Martin Haas

Astronomisches Institut, Ruhr Universität, D-44801 Bochum, Germany

Christian Leipski

Max-Planck Institut für Astronomie (MPIA), D-69117 Heidelberg, Germany

and

Belinda Wilkes

Harvard-Smithsonian Center for Astrophysics, Cambridge, MA 02138, USA

ABSTRACT

The unification model for powerful radio galaxies and radio-loud quasars postulates that these objects are intrinsically the same but viewed along different angles. *Herschel Space Observatory*¹ data permit the assessment of that model in the far-infrared spectral window. We analyze photometry from *Spitzer* and *Herschel* for the distant 3CR hosts, and find that radio galaxies and quasars have different mid-infrared, but indistinguishable far-infrared colors. Both these properties, the former being orientation dependent and the latter orientation invariant, are in line with expectations from the unification model. Adding powerful radio-quiet active galaxies and typical massive star-forming galaxies to the analysis, we demonstrate that infrared colors not only provide an orientation indicator, but can also distinguish active from star-forming galaxies.

¹*Herschel* is an ESA space observatory with science instruments provided by European-led Principal Investigator consortia and with important participation from NASA.

Subject headings: Galaxies: formation — Galaxies: active — Galaxies: starburst
— Galaxies: high-redshift — Infrared: galaxies

1. Introduction

Active Galactic Nuclei (AGN) show a large variety of observational properties despite being universally driven by accretion of matter onto supermassive black holes. Their ubiquitous nature and complex interplay with their host galaxies make AGN essential elements of any model of galaxy evolution. Since their discovery in the 1950s, AGN have been observationally classified into a number of different types depending on the particular wavelength range used for the observations. Unification models for AGN (Barthel 1989; Antonucci 1993; Urry & Padovani 1995) were developed later, explaining the differences between some AGN types solely in terms of viewing angle. An essential part of these models is the so-called AGN ‘torus’: a geometrically and optically thick structure filled with molecular gas and dust surrounding the active nucleus. The AGN torus has a geometry that allows radiation to escape freely in certain directions but not in others, rendering samples of objects selected at X-ray, ultra-violet (UV) and visible wavelengths largely inapplicable for testing unification models.

Radio-selected AGN are particularly well-suited for testing the unification model, because when selected based on their extended (well outside the torus), low-frequency, transparent (i.e. optically thin) radio emission they show no bias with respect to orientation. The unification model for powerful radio-loud AGN postulates that radio galaxies (RGs) are viewed edge-on so that the torus obscures the active nucleus and nearby broad-line emitting regions, while quasars (QSRs) are the same objects, but viewed with a face-on torus so that the nuclear regions and broad emission lines are directly visible. The validity of the unification model for powerful radio-loud AGN has been examined using a variety of orientation-dependent properties (recently reviewed in Antonucci 2012), in the radio (Barthel 1989; Singal 1993), mid-infrared (MIR) (Ogle et al. 2006; Cleary et al. 2007; Haas et al. 2008; Leipski et al. 2010), and X-ray (Wilkes et al. 2013) domains.

2. Infrared properties

If the unification model holds, then any isotropic (orientation invariant) property must be comparable for samples of RGs and QSRs with matched low-frequency radio properties. One such an isotropic candidate is the far-infrared (FIR) emission, which is dominated by star-formation-heated dust on the scale of the host galaxy, but may also include a con-

tribution from optically thin, AGN-powered emission from the torus. Due to sensitivity issues, earlier FIR studies relied on relatively small samples of mostly nearby, less luminous sources, and therefore failed to provide robust conclusions on the unification model for powerful radio-loud AGN in the FIR (e.g., Hes et al. 1995; van Bemmell et al. 2000; Meisenheimer et al. 2001; Haas et al. 2004). The *Herschel Space Observatory* (Pilbratt et al. 2010), with its unprecedented sensitivity, resolution, and wavelength coverage for the first time permits rest-frame FIR tests of unification for distant radio-loud AGN which have hitherto been outside the reach of infrared space missions. In order to test the unification model in the FIR, we study the complete $z > 1$ 3CR sample of powerful ($L_{178\text{MHz}} > 5 \times 10^{28} \text{ W Hz}^{-1}$) radio-loud AGN (Spinrad et al. 1985) using the two *Herschel* imaging photometers: PACS at 70 and 160 μm (Poglitsch et al. 2010) and SPIRE at 250, 350, and 500 μm (Griffin et al. 2010). The extreme luminosities of our sample objects ensure that all objects are highly accreting (in quasar-mode, e.g., Best & Heckman 2012); none of them is classified as a low-ionization emission-line source (e.g., Ogle et al. 2006).

In addition to the *Herschel* data, the availability of ancillary *Spitzer* (Werner et al. 2004) data at wavelengths between 3.6 and 24 μm (Haas et al. 2008) allows us to obtain physical properties of the 3CR hosts by fitting their full infrared spectral energy distributions (SEDs) with a combination of four components, as explained in detail in Barthel et al. (2012) and Podigachoski et al. (2015). These components include emission from the circumnuclear, AGN-heated torus dust (Hönig & Kishimoto 2010), from the extended star-formation-heated cold dust, from the evolved stellar populations, and from hot nuclear graphite dust. The best-fit SEDs of our 61 3CR hosts were recently presented in Podigachoski et al. (2015). Twenty-three hosts in the sample (presented in Table 1) have good signal-to-noise detections in at least three *Herschel* bands, typically the three shortest bands, resulting in estimated star formation rates (SFRs) of order hundreds of solar masses per year, coeval with the black hole activity (Podigachoski et al. 2015). Such prodigious SFRs, at the level of ultra-luminous infrared galaxies, have similarly been inferred in other studies of high- z radio galaxies (e.g. Ogle et al. 2012; Drouart et al. 2014; Tadhunter et al. 2014).

3. MIR/FIR colors – a powerful tool

A simpler but revealing way to look at the shapes of SEDs is to employ colors. Infrared color-color diagrams are widely used to separate AGN from non-AGN in wide-/deep-field galaxy surveys (e.g., Lacy et al. 2004; Stern et al. 2005; Donley et al. 2012; Kirkpatrick et al. 2013). Using the best-fit SEDs of the 23 3CR objects detected in at least three *Herschel* bands, we create rest-frame color-color diagrams from their hosts’ dust emission at 5, 20,

70, and 100 μm . The emission at the former two wavelengths is mainly AGN-powered (e.g., Rowan-Robinson 1995), whereas the emission at the latter two wavelengths is predominantly star-formation-powered (Schweitzer et al. 2006).

In Fig. 1 we show infrared color-color diagrams for this sample of 13 RGs and 10 QSRs. The distributions of $F_{100\mu\text{m}}/F_{70\mu\text{m}}^2$ color for RGs and QSRs in Fig. 1 are nearly identical, with median values 0.9. The color coding in Fig. 1 (left) demonstrates that the factor of ~ 2 scatter around the median FIR colors results from differences in the cold dust temperatures of individual objects, which range from ~ 25 to ~ 45 K (Podigachoski et al. 2015). The emission from hosts with dust temperatures < 33 K peaks at wavelengths > 70 μm resulting in $F_{100\mu\text{m}}/F_{70\mu\text{m}} > 1$. We apply both maximum likelihood and empirical methods to statistically compare the measured RG and QSR $F_{100\mu\text{m}}/F_{70\mu\text{m}}$ colors. Assuming that the colors are normally distributed, we compute the parameters of the distributions which maximize the probability of measuring such colors. The means and standard deviations of these maximum likelihood distributions are 1.0 and 0.2, respectively, for both the RGs and QSRs. The corresponding maximum likelihood cumulative distribution functions and the empirical (measured) cumulative distributions are presented in Fig. 2 (left). The Kolmogorov-Smirnov (KS) test reveals that the two samples are drawn from the same distribution ($\text{KS}_{\text{statistic}}=0.07$, $p=1$). We conclude that the FIR colors of these 3CR RGs and QSRs are indistinguishable (i.e., orientation invariant), as expected in the unification model for AGN host galaxies with similar star formation rates.

In contrast, the RGs and QSRs show clear separation in their $F_{70\mu\text{m}}/F_{5\mu\text{m}}$ colors (Fig. 1, left): their median colors are 101.4 and 13.9, respectively. One RG, 3C 119, has colors which overlap the QSRs in Fig. 1 (left), not surprisingly, because 3C 119 is a well-known (de Vries et al. 1997) borderline source where some of the hot dust is visible, and the UV/visible AGN continuum is only partly hidden. The 5 μm emission of another RG, 3C 222, is only weakly constrained (Podigachoski et al. 2015), resulting in an unusually red $F_{70\mu\text{m}}/F_{5\mu\text{m}}$ color for this object. Considering this particular value as an upper limit, we obtain $\text{KS}_{\text{statistic}}=0.92$ ($p=5\times 10^{-5}$), and maximum likelihood distributions as plotted in Fig. 2 (middle). These clearly different distributions are driven by the differences between the RG and QSR SEDs at 5 μm . RGs are fainter than QSRs at 5 μm , as expected if their hot inner torus dust emission is obscured due to its edge-on viewing angle (Haas et al. 2008; Leipski et al. 2010; Dicken et al. 2014). Our results support the hypothesis that $F_{70\mu\text{m}}/F_{5\mu\text{m}}$ to a large extent reveals the level of obscuration in powerful radio-loud objects, and as such is an orientation indicator for that AGN population. However, intrinsic differences in this ratio for individual

²monochromatic flux densities are given in units of $\text{erg s}^{-1} \text{cm}^{-2} \text{Hz}^{-1}$

objects are not ruled out, and may contribute to the observed scatter.

Although our adopted SED-fitting approach is physically grounded and provides us with a close approximation of the objects’ infrared SEDs, we further explore the robustness of the results presented above without using dust emission models. To this end, we employ a simple (model-independent) linear interpolation of the observed flux values to obtain the rest-frame colors and create the color-color diagrams. We apply this method to the sample of objects detected in at least three *Herschel* bands, and find that the RGs and QSRs remain clearly separated in the $F_{70\mu\text{m}}/F_{5\mu\text{m}}$ color, with median values of 83.9 and 12.3, respectively. Their respective median $F_{100\mu\text{m}}/F_{70\mu\text{m}}$ colors (1.0 and 0.9) remain indistinguishable, similarly to the results obtained when following the SED-fitting approach.

In addition to the 23 3CR hosts detected in at least three *Herschel* bands, seven hosts are detected in only the two PACS bands while remaining below the detection limit in the SPIRE bands. Given the low redshift range ($1 < z \leq 1.35$) of five of these seven hosts, the PACS 160 μm band probes their cold dust emission at rest-frame $\sim 70 \mu\text{m}$ allowing their inclusion (empty symbols) in the color-color diagrams presented in Fig. 1. While this inclusion does not change the trends discussed above, their $F_{70\mu\text{m}}/F_{5\mu\text{m}}$ colors tend to be somewhat bluer than the median colors of the 23 objects detected in at least three *Herschel* bands. This is likely a consequence of their lower levels of star formation (Podigachoski et al. 2015). As such, it is important to note that the present FIR test of unification can directly be applied only to the long wavelength detected, i.e., the star-forming objects from the high- z 3CR sample. The 31 remaining hosts from the sample, which are either detected only in the PACS 70 μm band or not detected at all, have weak or absent star formation and thus no definitive conclusions can be drawn. Nevertheless, the non-detection fractions at SPIRE 250 μm for RGs and QSRs are comparable ($\sim 65\%$ and $\sim 58\%$ respectively), and thus do not represent evidence against the unification model.

The high level of obscuration in the MIR prevents the $F_{70\mu\text{m}}/F_{5\mu\text{m}}$ color from directly probing the relative importance of the SF and AGN activity. We therefore use the AGN-powered circumnuclear dust emission at 20 μm (near the peak emission from the torus, e.g., Hönic & Kishimoto 2010), and employ the $F_{70\mu\text{m}}/F_{20\mu\text{m}}$ color to probe the dominant power source in the infrared. As shown in Fig. 1 (right), the $F_{70\mu\text{m}}/F_{20\mu\text{m}}$ RG and QSR colors are closer to each other than the $F_{70\mu\text{m}}/F_{5\mu\text{m}}$ colors, but still have an offset, with median values of 3.4 and 1.8 respectively ($K_{\text{S}_{\text{statistic}}}=0.65$, $p=0.01$; see Fig. 2, right), confirming that the level of obscuration at 20 μm is substantially lower than that at 5 μm . The symbols in Fig. 1 (right) are color-coded according to the fractional star formation luminosity, $L_{\text{SF}}/L_{\text{IR}}$, as inferred in Podigachoski et al. (2015). This color-coding demonstrates that, despite the strong star formation activity of several hundreds of solar masses per year, the total infrared

luminosity of the 3CR hosts is generally dominated by their AGN activity, regardless if that activity is obscured or not (Podigachoski et al. 2015). The only exceptions are two RGs, 3C 266 and 3C 222, which have similar L_{SF} but lower IR AGN luminosities than the other RGs (Podigachoski et al. 2015). However, a general increase in the $L_{\text{SF}}/L_{\text{IR}}$ ratio of 3CR objects, from $\sim 10\%$ to $\sim 60\%$, is observed when progressing to larger $F_{70\mu\text{m}}/F_{20\mu\text{m}}$ values, i.e., to redder colors.

We examine this trend further by comparing the 3CR AGN infrared colors to those of typical star-forming (SF) galaxies where the infrared emission draws uniquely from star formation. The SFR strongly correlates with stellar mass and redshift (Elbaz et al. 2007); we therefore select $z \sim 2$ SF galaxies from Kirkpatrick et al. (2012) with stellar masses and redshifts comparable to those of the 3CR hosts (which have $M_{\text{stellar}} \gtrsim 10^{11} M_{\odot}$, e.g., Best et al. 1998; De Breuck et al. 2010). Given that stars in these SF galaxies are formed at rates (Kirkpatrick et al. 2012) comparable to those in the 3CR hosts, the $L_{\text{SF}}/L_{\text{IR}} \sim 1$ of the SF galaxies are consistent with their red $F_{70\mu\text{m}}/F_{20\mu\text{m}}$ colors (Fig. 1 right). The bluer $F_{70\mu\text{m}}/F_{20\mu\text{m}}$ colors of the powerful 3CR AGN are likely a consequence of the strong torus emission at $20 \mu\text{m}$. The average cold dust temperature of the SF galaxies is 28 ± 2 K (Kirkpatrick et al. 2012), hence their FIR colors are also consistent with the temperature trends found for the 3CR hosts. The $F_{70\mu\text{m}}/F_{20\mu\text{m}}$ colors of powerful AGN are offset from those of SF galaxies, and hence, in addition to being indicators of orientation, FIR/MIR colors also distinguish between active and SF galaxies in the most luminous star-forming objects, analogous to the case for local Seyfert galaxies (e.g., de Grijp et al. 1985).

A limitation for the general unification discussion is the fact that radio-loud AGN, such as the 3CR sources investigated here, represent a small ($\sim 10\%$) fraction of the complete AGN population. It is therefore important to compare the colors of the powerful 3CR radio-loud AGN to those of powerful radio-quiet AGN. To achieve this, we select a sample of distant ($z_{\text{med}} \sim 1.9$), luminous, radio-quiet AGN ($L_{2-10\text{keV}} \sim 5 \times 10^{44} \text{ erg s}^{-1}$) hosted by massive ($M_{\text{stellar}} \sim 10^{11} M_{\odot}$) star-forming galaxies, from Kirkpatrick et al. (2012). As shown in Fig. 1 (right) the radio-quiet AGN have $F_{70\mu\text{m}}/F_{20\mu\text{m}}$ colors redder than those of the 3CR RGs, but bluer than those of the SF galaxies. Given that the SF activity in these radio-quiet AGN accounts for 56% of the total infrared luminosity (Kirkpatrick et al. 2012), this finding agrees with the trend of increasing $L_{\text{SF}}/L_{\text{IR}}$ towards larger $F_{70\mu\text{m}}/F_{20\mu\text{m}}$ values for the 3CR objects discussed above.

4. Conclusion

In conclusion, far- to mid-infrared colors represent a useful diagnostic of the orientation of powerful radio-loud AGN, and support the unification model for these objects. At wavelengths longer than $20\ \mu\text{m}$, where obscuration is a small effect, these colors are also indicators of the relative contributions of star formation and nuclear activity in galaxies. These diagnostics may prove useful in future studies of large samples of dusty star-forming galaxies/AGN to investigate the duty cycle of nuclear activity, feedback, and AGN and galaxy growth.

We thank the referee, Patrick Ogle, for a very constructive report which improved the manuscript. Data were taken from the *Herschel* Guaranteed Time project *The Herschel Legacy of distant radio-loud AGN* (PI: PB). PP acknowledges the Nederlandse Organisatie voor Wetenschappelijk Onderzoek (NWO) for a PhD fellowship. The *Herschel* spacecraft was designed, built, tested, and launched under a contract to ESA managed by the *Herschel/Planck* Project team by an industrial consortium under the overall responsibility of the prime contractor Thales Alenia Space (Cannes), and including Astrium (Friedrichshafen) responsible for the payload module and for system testing at spacecraft level, Thales Alenia Space (Turin) responsible for the service module, and Astrium (Toulouse) responsible for the telescope, with in excess of a hundred subcontractors. PACS has been developed by a consortium of institutes led by MPE (Germany) and including UVIE (Austria); KU Leuven, CSL, IMEC (Belgium); CEA, LAM (France); MPIA (Germany); INAF-IFSI/OAA/OAP/OAT, LENS, SISSA (Italy); IAC (Spain). This development has been supported by the funding agencies BMVIT (Austria), ESA-PRODEX (Belgium), CEA/CNES (France), DLR (Germany), ASI/INAF (Italy), and CICYT/MCYT (Spain). SPIRE has been developed by a consortium of institutes led by Cardiff University (UK) and including Univ. Lethbridge (Canada); NAOC (China); CEA, LAM (France); IFSI, Univ. Padua (Italy); IAC (Spain); Stockholm Observatory (Sweden); Imperial College London, RAL, UCL-MSSL, UKATC, Univ. Sussex (UK); and Caltech, JPL, NHSC, Univ. Colorado (USA). This development has been supported by national funding agencies: CSA (Canada); NAOC (China); CEA, CNES, CNRS (France); ASI (Italy); MCINN (Spain); SNSB (Sweden); STFC, UKSA (UK); and NASA (USA). This work is partly based on observations made with the *Spitzer* Space Telescope, which is operated by the Jet Propulsion Laboratory, California Institute of Technology under a contract with NASA.

Facilities: Herschel, Spitzer.

REFERENCES

- Antonucci, R. 1993, *ARA&A*, 31, 473
- Antonucci, R. 2012, *Astronomical and Astrophysical Transactions*, 27, 557
- Barthel, P. D. 1989, *ApJ*, 336, 606
- Barthel, P., Haas, M., Leipski, C., & Wilkes, B. 2012, *ApJ*, 757, LL26
- Best, P. N., Longair, M. S., & Roettgering, H. J. A. 1998, *MNRAS*, 295, 549
- Best, P. N., & Heckman, T. M. 2012, *MNRAS*, 421, 1569
- Cleary, K., Lawrence, C. R., Marshall, J. A., Hao, L., & Meier, D. 2007, *ApJ*, 660, 117
- De Breuck, C., Seymour, N., Stern, D., et al. 2010, *ApJ*, 725, 36
- de Grijp, M. H. K., Miley, G. K., Lub, J., & de Jong, T. 1985, *Nature*, 314, 240
- de Vries, W. H., O’Dea, C. P., Baum, S. A., et al. 1997, *ApJS*, 110, 191
- Dicken, D., Tadhunter, C., Morganti, R., et al. 2014, *ApJ*, 788, 98
- Donley, J. L., Koekemoer, A. M., Brusa, M., et al. 2012, *ApJ*, 748, 142
- Drouart, G., De Breuck, C., Vernet, J., et al. 2014, *A&A*, 566, AA53
- Elbaz, D., Daddi, E., Le Borgne, D., et al. 2007, *A&A*, 468, 33
- Griffin, M. J., Abergel, A., Abreu, A., et al. 2010, *A&A*, 518, LL3
- Haas, M., Müller, S. A. H., Bertoldi, F., et al. 2004, *A&A*, 424, 531
- Haas, M., Willner, S. P., Heymann, F., et al. 2008, *ApJ*, 688, 122
- Hes, R., Barthel, P. D., & Hoekstra, H. 1995, *A&A*, 303, 8
- Hönig, S. F., & Kishimoto, M. 2010, *A&A*, 523, AA27
- Kirkpatrick, A., Pope, A., Alexander, D. M., et al. 2012, *ApJ*, 759, 139
- Kirkpatrick, A., Pope, A., Charmandaris, V., et al. 2013, *ApJ*, 763, 123
- Lacy, M., Storrie-Lombardi, L. J., Sajina, A., et al. 2004, *ApJS*, 154, 166
- Leipski, C., Haas, M., Willner, S. P., et al. 2010, *ApJ*, 717, 766

- Meisenheimer, K., Haas, M., Müller, S. A. H., et al. 2001, *A&A*, 372, 719
- Ogle, P., Whysong, D., & Antonucci, R. 2006, *ApJ*, 647, 161
- Ogle, P., Davies, J. E., Appleton, P. N., et al. 2012, *ApJ*, 751, 13
- Pilbratt, G. L., Riedinger, J. R., Passvogel, T., et al. 2010, *A&A*, 518, LL1
- Podigachoski, P., Barthel, P. D., Haas, M., et al. 2015, *A&A*, 575, AA80
- Poglitsch, A., Waelkens, C., Geis, N., et al. 2010, *A&A*, 518, LL2
- Rowan-Robinson, M. 1995, *MNRAS*, 272, 737
- Schweitzer, M., Lutz, D., Sturm, E., et al. 2006, *ApJ*, 649, 79
- Singal, A. K. 1993, *MNRAS*, 262, L27
- Spinrad, H., Marr, J., Aguilar, L., & Djorgovski, S. 1985, *PASP*, 97, 932
- Stern, D., Eisenhardt, P., Gorjian, V., et al. 2005, *ApJ*, 631, 163
- Tadhunter, C., Dicken, D., Morganti, R., et al. 2014, *MNRAS*, 445, L51
- Urry, C. M., & Padovani, P. 1995, *PASP*, 107, 803
- van Bemmell, I. M., Barthel, P. D., & de Graauw, T. 2000, *A&A*, 359, 523
- Werner, M. W., Roellig, T. L., Low, F. J., et al. 2004, *ApJS*, 154, 1
- Wilkes, B. J., Kuraszkiewicz, J., Haas, M., et al. 2013, *ApJ*, 773, 15

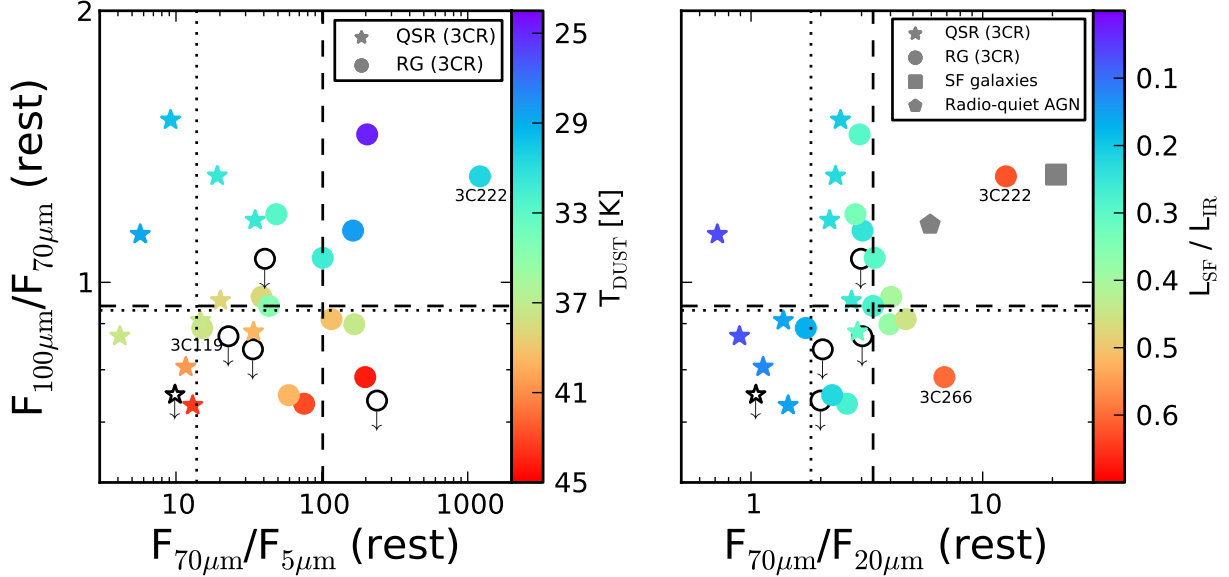


Fig. 1.— Rest-frame infrared color-color diagrams computed by fitting a multi-component model to the observed spectral energy distributions of the 3CR objects. The ordinate represents $F_{100\mu\text{m}}/F_{70\mu\text{m}}$ color in both plots, the abscissa the $F_{70\mu\text{m}}/F_{5\mu\text{m}}$ (left plot) and $F_{70\mu\text{m}}/F_{20\mu\text{m}}$ color (right plot). The 3CR quasars are shown with stars, the 3CR radio galaxies with circles. Filled colored symbols represent objects detected in at least three *Herschel* bands, whereas empty symbols represent objects detected in only the two shortest *Herschel* bands, for which $F_{100\mu\text{m}}$ is estimated as an upper limit. Dotted and dashed lines mark the corresponding median colors of quasars and radio galaxies, respectively. In the left plot, the 3CR objects are color-coded according to their cold dust temperatures, T_{DUST} , as found from the SED-fitting. The T_{DUST} scale is indicated in the left vertical color bar. In the right plot, the 3CR objects are color-coded according to their fractional star formation luminosity, $L_{\text{SF}}/L_{\text{IR}}$. The $L_{\text{SF}}/L_{\text{IR}}$ scale is indicated in the right vertical color bar. T_{DUST} and $L_{\text{SF}}/L_{\text{IR}}$ are listed in Table 1. Grey symbols show the median colors of the comparison star-forming galaxies at $z \sim 2$ (square) and radio-quiet AGN (pentagon), both from Kirkpatrick et al. (2012).

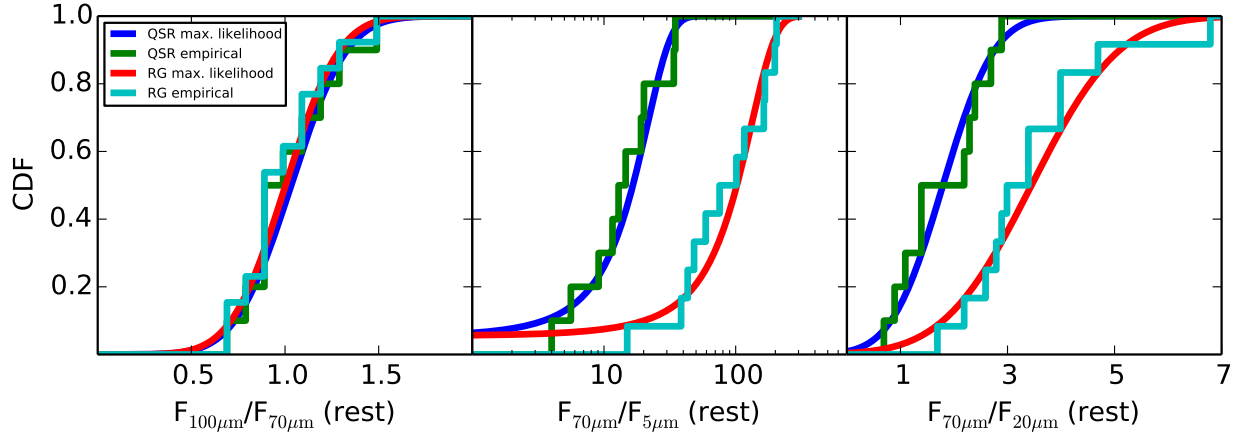


Fig. 2.— Maximum likelihood and empirical (measured) cumulative distribution functions of $F_{100\mu\text{m}}/F_{70\mu\text{m}}$ (left), $F_{70\mu\text{m}}/F_{5\mu\text{m}}$ (middle), and $F_{70\mu\text{m}}/F_{20\mu\text{m}}$ (right) colors of the 3CR objects. Quasars (blue/green) and radio galaxies (red/cyan) have different $F_{70\mu\text{m}}/F_{5\mu\text{m}}$ and $F_{70\mu\text{m}}/F_{20\mu\text{m}}$ distributions and indistinguishable $F_{100\mu\text{m}}/F_{70\mu\text{m}}$ distributions, both in line with expectations from the unification model of radio-loud AGN. (Left) Parameters of quasar maximum likelihood distribution: $\mu=1.0$, $\sigma=0.2$. Parameters of radio galaxy maximum likelihood distribution: $\mu=1.0$, $\sigma=0.2$. (Middle) Parameters of quasar maximum likelihood distribution: $\mu=16.6$, $\sigma=10.2$. Parameters of radio galaxy maximum likelihood distribution: $\mu=102.1$, $\sigma=63.9$. (Right) Parameters of quasar maximum likelihood distribution: $\mu=1.8$, $\sigma=0.7$. Parameters of radio galaxy maximum likelihood distribution: $\mu=3.4$, $\sigma=1.3$. 3C 222 has not been included in the $F_{70\mu\text{m}}/F_{5\mu\text{m}}$ and $F_{70\mu\text{m}}/F_{20\mu\text{m}}$ distributions of radio galaxies (see text).

Table 1. Properties of the 3CR objects plotted in Fig. 1. The top 23 objects are detected in at least three *Herschel* bands, whereas the bottom 5 objects in only two *Herschel* bands. The redshifts of the objects are taken from Spinrad et al. (1985). Columns 4 through 8 are computed by fitting the full infrared spectral energy distributions of the hosts as described in the text.

Name	Type	z	$F_{70\mu\text{m}}/F_{5\mu\text{m}}$	$F_{70\mu\text{m}}/F_{20\mu\text{m}}$	$F_{100\mu\text{m}}/F_{70\mu\text{m}}$	T_{DUST} [K]	$L_{\text{SF}}/L_{\text{IR}}$
3C 002	QSR	1.04	19.2	2.3	1.3	31.6	0.23
3C 014	QSR	1.47	4.1	0.9	0.9	37.5	0.08
3C 068.2	RG	1.57	163.7	3.0	1.1	28.5	0.25
3C 119	RG	1.02	15.1	1.7	0.9	37.6	0.17
3C 124	RG	1.08	101.4	3.4	1.1	31.9	0.30
3C 190	QSR	1.20	34.9	2.2	1.2	31.7	0.23
3C 205	QSR	1.53	11.7	1.1	0.8	40.7	0.13
3C 222	RG	1.34	1212.7	12.6	1.3	30.6	0.62
3C 245	QSR	1.03	5.7	0.7	1.1	28.8	0.07
3C 256	RG	1.82	75.6	2.6	0.7	43.0	0.27
3C 257	RG	2.47	38.6	4.0	1.0	38.2	0.40
3C 266	RG	1.27	198.3	6.8	0.8	44.2	0.60
3C 270.1	QSR	1.52	13.0	1.4	0.7	43.5	0.15
3C 297	RG	1.41	204.5	2.9	1.5	24.9	0.30
3C 298	QSR	1.44	14.7	1.4	0.9	37.5	0.16
3C 305.1	RG	1.13	43.4	3.4	0.9	34.7	0.28
3C 318	QSR	1.57	34.0	2.9	0.9	39.6	0.31
3C 324	RG	1.21	59.3	2.2	0.7	39.6	0.23
3C 368	RG	1.13	166.8	4.0	0.9	37.3	0.38
3C 432	QSR	1.80	9.2	2.4	1.5	29.8	0.21
3C 454.0	QSR	1.76	20.2	2.7	1.0	38.3	0.26
3C 454.1	RG	1.84	116.4	4.7	0.9	39.3	0.45
3C 470	RG	1.65	48.4	2.8	1.2	32.8	0.34
Objects detected in only two <i>Herschel</i> bands							
3C 013	RG	1.35	238.8	2.0	<0.7		
3C 210	RG	1.17	40.7	3.0	<1.1		
3C 220.2	QSR	1.16	9.8	1.0	<0.8		
3C 356	RG	1.08	33.7	2.0	<0.8		
3C 469.1	RG	1.34	22.9	3.0	<0.9		